



# Efficient photothermal degradation on $\text{Bi}_{12}\text{CoO}_{20}$ sillenite with a strong internal electric field induced by the thermal effect



Zhenlin Wang <sup>a,b</sup>, Yanying Wang <sup>a,b</sup>, Yaning Zhang <sup>a,b</sup>, Xue Sun <sup>a,b</sup>, Yang Lou <sup>a,b</sup>, Ying Zhang <sup>a,b</sup>, Yuming Dong <sup>a,b</sup>, Chengsi Pan <sup>a,b,\*</sup>, Yongfa Zhu <sup>a,b,c,d,\*</sup>

<sup>a</sup> Key Laboratory of Synthetic and Biological Colloids, Ministry of Education, School of Chemical and Material Engineering, Jiangnan University, Wuxi, Jiangsu 214122, China

<sup>b</sup> International Joint Research Center for Photoresponsive Molecules and Materials, Jiangnan University, Wuxi, Jiangsu 214122, China

<sup>c</sup> School of Food Science and Technology, Jiangnan University, Wuxi, Jiangsu 214122, China

<sup>d</sup> Department of Chemistry, Tsinghua University, Beijing 100084, China

## ARTICLE INFO

### Keywords:

Photothermal effect  
Internal electric field  
Bismuth-based photocatalyst  
Wide-spectrum responsive  
Phenols

## ABSTRACT

A novel sillenite,  $\text{Bi}_{12}\text{CoO}_{20}$ , is reported to effectively utilize a large portion of the solar spectrum up to the Near-IR region (1000 nm), and exhibits excellent photothermal degradation. The degradation is evaluated by using phenol as the model pollutant and correlated with a temperature-induced structure change through in-situ photoelectrochemical and spectroscopic characterizations. The degradation rate on  $\text{Bi}_{12}\text{CoO}_{20}$  is ca. 3.0 times higher than that on P25-TiO<sub>2</sub> under simulated sunlight irradiation and the best by comparing with other reported photothermal catalysts. The thermal effect is demonstrated to cause the conversion of  $\text{Co}^{3+}$  to  $\text{Co}^{2+}$  at the octahedral sites of the  $\text{Bi}_{12}\text{CoO}_{20}$ , increase the internal electric field, and facilitate charge separation. The conversion also positively shifts the band potential, increasing the oxidative reactive species. The photothermal activity is newly found to be enhanced by increasing the IEF and band edge potential, which may provide strategies for designing more effective photothermal catalysts.

## 1. Introduction

Photodegradation has been widely studied in the environmental remediation field due to its energy-saving and renewable characteristics [1]. However, current photocatalysts exhibit low activity under wide-solar-spectrum irradiation and suffer from an insufficient solar-energy conversion rate. Insufficiently utilized solar energy is mainly lost when unused infrared (IR) light is transformed into heat [2]. If the released heat could be reutilized, the photocatalytic activity under wide-solar-spectrum irradiation would be significantly enhanced. Therefore, the development of photothermal catalysts that can efficiently utilize released heat is of much interest, as it will enable sufficient sunlight utilization [3,4].

In previous studies, photothermal catalysts that can utilize heat from IR light have been developed, and they showed superior activity for the removal of VOCs [5,6]; they have included carbon-based materials, plasma cocatalyst-decorated photocatalysts, and Mn-based/Co-based oxides [7–9]. These pioneering studies showed that during the

degradation of gaseous pollutants, the energy lost in the form of heat can be collected efficiently and reused to enhance photocatalytic activity. However, in the case of pollutant degradation in wastewater, photothermal catalysts have not been sufficiently developed to degrade VOCs because water possesses a specific heat capacity ( $4.2 \times 10^3 \text{ J} (\text{kg } ^\circ\text{C})^{-1}$ ) nearly 4 times higher than that of air [10], leading to the limited efficiency of the enhancement of photocatalyst surface temperature by released heat and the accompanying surface-temperature-induced charge transfer. In addition, most previous studies focused on the enhancement of the surface charge capture by pollutants due to the photothermal effect [11,12]. The effect of photothermal treatment on the change in the inherent structure of photocatalysts and the relationship with the relevant promotion of charge separation remain unclear.

Bi-based photocatalysts are a series of materials with excellent activity for degrading various organic pollutants, such as dyes and phenols, in aqueous solution [13–16]. However, these materials have rarely been studied as photothermal catalysts because most of the Bi-based

\* Corresponding authors at: Key Laboratory of Synthetic and Biological Colloids, Ministry of Education, School of Chemical and Material Engineering, Jiangnan University, Wuxi, Jiangsu 214122, China.

E-mail addresses: [cspan@jiangnan.edu.cn](mailto:cspan@jiangnan.edu.cn) (C. Pan), [zhuyf@tsinghua.edu.cn](mailto:zhuyf@tsinghua.edu.cn) (Y. Zhu).

photocatalyst responses are far below the IR region (approximately 550 nm), and cannot utilize the IR-produced heat. Although some modification methods, such as heterojunction-construction or cation-doping, can extend the adsorption edge into the IR region ( $\text{Bi}_2\text{S}_3/\text{Bi}_2\text{WO}_6$  [17] or Fe-doped  $\text{BiOI}$  [18]), modified Bi-based photocatalysts still show negligible photothermal effects, probably due to the lack of a suitable structure for eliciting an efficient photothermal response.

Co-based photocatalysts are photocatalysts that usually absorb in the IR region and efficiently perform photothermal synergistic degradation; they include the reported  $\text{Co}_3\text{O}_4$  and  $\text{Co}_2\text{C}$  photothermal catalysts [8, 19]. The 3d orbitals of Co commonly contribute to band edge and overlap easily with other atoms in the coordination environment, which narrows the bandgap and extends the light harvesting to the IR region [20]. Therefore, Co-based photocatalysts are considered good candidates for photothermal catalysts. However, Co-based photocatalysts usually exhibit many defects, which act as recombination centers, and suffer from photocorrosion. These drawbacks cause rather low intrinsic photoactivity of Co-based photocatalysts and limit the subsequent photothermal enhancement on the basis of the low intrinsic activity.

In our previous work, a new sillenite photocatalytic system was successfully prepared via complete co-substitution at the tetrahedral sites of the sillenite ( $\text{Bi}_{12}\text{SiO}_{20}$ ) with  $\text{Bi}^{5+}$  and  $\text{Co}^{3+}$  cations [21]. The sillenite photocatalytic system was versatile for co-substitution with different Bi: Co ratios. The typical photocatalyst in the developed sillenite system,  $\text{Bi}_{24}(\text{Bi}^{\text{V}}\text{Co}^{\text{III}})\text{O}_{40}$ , contains  $\text{Co}^{3+}$  in the lattice and showed superior intrinsic activity compared to other Co-based photocatalysts for the degradation of dyes at room temperature. The photocatalyst also showed a photo response up to 750 nm near the IR region. These advantages suggest that with further tuning of the substituted Bi: Co ratios, the Bi-Co-O sillenite photocatalytic system may be suitable for photothermal degradation.

Herein, a sillenite photocatalyst,  $\text{Bi}_{12}\text{CoO}_{20}$  ( $(\text{Bi}_{11.5}^{\text{III}}\text{Co}_{0.5}^{\text{III}})(\text{Bi}_{0.5}^{\text{V}}\text{Co}_{0.5}^{\text{III}})\text{O}_{20}$ ) with a new Bi: Co ratio relative to the reported  $\text{Bi}_{24}(\text{Bi}^{\text{V}}\text{Co}^{\text{III}})\text{O}_{40}$ , was prepared by a hydrothermal method. The photocatalyst exhibits a wide-spectrum response up to 1000 nm. The newly designed structure is simplified by the fact that  $\text{Co}^{3+}$  occupies not only tetrahedral sites, as reported in  $\text{Bi}_{24}(\text{Bi}^{\text{V}}\text{Co}^{\text{III}})\text{O}_{40}$  but also octahedral sites. The prepared  $\text{Bi}_{12}\text{CoO}_{20}$  photocatalyst exhibited superior photothermal activity under simulated sunlight irradiation compared to typical photocatalysts ( $\text{P25-TiO}_2$ ,  $\text{g-C}_3\text{N}_4$ ,  $\text{Bi}_2\text{WO}_6$ ) and the reported  $\text{Bi}_{24}(\text{Bi}^{\text{V}}\text{Co}^{\text{III}})\text{O}_{40}$  under the same photothermal conditions. The thermal effect on the lattice structure, dipole-induced internal electric field (IEF), charge separation, and band structure was investigated by in-situ and ex-situ electrochemical, spectroscopic, and DFT calculation methods. The relationship between the photodegradation enhancement and the thermal effect-induced conversion of  $\text{Co}^{3+}$  to  $\text{Co}^{2+}$  at the octahedral sites of the sillenite has been clarified. The study of this system provides a strategy for enhancing the IEF and activity of photocatalysts by the thermal effect.

## 2. Experimental section

All chemicals (AR grade) were purchased from the National Chemical Company (Shanghai, China) and used without further purification. Ultrapure water of 18.2 MΩ was employed for all the experiments.

### 2.1. Synthesis of $\text{Bi}_{12}\text{CoO}_{20}$ photocatalyst

1.2 mmol  $\text{Bi}(\text{NO}_3)_3 \bullet 5 \text{ H}_2\text{O}$  and 0.1 mmol  $\text{Co}(\text{NO}_3)_2 \bullet 6 \text{ H}_2\text{O}$  were added into 20 ml water in sequence. Then 10 ml NaOH aq (12 M) was dropped into the solution with stirring and formed a pale-yellow suspension. The suspension was kept at room temperature and stirred for another 30 min and then transferred to a 50 ml Para polyphenol-sealed stainless-steel autoclave. The autoclave was maintained at 270 °C for 24 h and then cooled down to room temperature. After the reaction, the product was washed with water and ethanol until pH= 7 and dried at

60 °C overnight. The obtained sample was ball-milled at 1400 rpm for 1 h before use. The photocatalysts with other ratios of Bi and Co were prepared in a similar method.

### 2.2. Characterization of $\text{Bi}_{12}\text{CoO}_{20}$

X-ray diffraction (XRD, Bruker D8-ADVANCE X-ray diffractometer German) at 40 kV and 40 mA with a Cu K $\alpha$  monochromator was used to characterize the crystal structure. The scanning (SEM, Hitachi S-4800, Japan) and transmission electron microscopy (TEM, JEM 2100plus, JEOL, Japan) were used to characterize the morphology. The Brunauer-Emmett-Teller (BET) surface was measured on a nitrogen absorption-desorption facility at 77 K (Micromeritics, ASAP2020 MP). UV-vis spectrophotometer (UV-3600 plus, Shimadzu, Japan) was used to record the absorption. The ICP was studied by ICP-AES (PE optima 8000).

### 2.3. Evaluation of photothermal degradation activity

Photothermal degradation activity of the prepared  $\text{Bi}_{12}\text{CoO}_{20}$  sample was evaluated via the degradation of phenols (phenol, bisphenol A, 4-chlorophenol, catechol, 2,4-dichlorophenol, 5 ppm, 50 ml) under a 300 W Xe lamp with an AM 1.5 filter (Perfect Light, Beijing, China). The reactor during the degradation was without cooling water, and the temperature of the suspension was raised by the light heat from the Xe lamp. After irradiating the suspension for 20 min, the temperature of the suspension reached thermal equilibrium, and then the pollutants were added to the solution to start the photothermal degradation. During the degradation, the temperature fluctuation is less than 5 °C. The average light intensity was 100 mW cm<sup>-2</sup> and the photocatalyst concentration was 0.5 g/L in the solution. To clarify the influence of the photothermal effect, accurate temperature (15 °C, 30 °C, 45 °C and 60 °C) was controlled in an electric-heated thermostatic water bath or by cooling water according to the cases. The temperature derivation in this case is ± 1 °C.

Before reaction, the suspension was ultrasonicated for 10 min to disperse. During the detection process, 1 ml suspension was sampled at a specific time and filtrated with 0.45 μm Navigator filter to remove particles. The high-performance liquid chromatography (HPLC, Ultimate 3000 RS, Japan) monitored at 270 nm and equipped with a C18 reverse-phase column was used to test the concentration of phenol solution. The flow rate of the mobile phase (V<sub>methanol</sub>: V<sub>water</sub> = 7: 3) was 1.0 ml min<sup>-1</sup>.

### 2.4. Photo-thermo electrochemical test

To test the photo-thermo electrochemical properties, the electrolyte temperature was kept at 60 °C and 25 °C, respectively, by a hot plate. Transient photocurrent, electrochemical impedance and open circuit potential measurements were employed to test the photo-thermo electrochemical properties. The measurements were performed on an electrochemical work station (CHI 750E, Chenzhua, Shanghai, China). A three-electrode system was used in the process. The working electrode was photocatalysts/FTO; the counter electrode was a platinum net, and the reference electrode was the standard Ag/AgCl electrode (E = 0.210 V vs. NHE). During the test, 0.5 M  $\text{Na}_2\text{SO}_4$  was used as the electrolyte, and the light source was offered by a 300 W Xe lamp. The working electrode of the  $\text{Bi}_{12}\text{CoO}_{20}$  catalyst was cast on an FTO glass via a drop-coating method. 3 mg  $\text{Bi}_{12}\text{CoO}_{20}$  catalyst was dispersed in 100 μL H<sub>2</sub>O to form a homogeneous slurry. The slurry was dropped onto the FTO glass (1 cm × 1 cm) and dried at 25 °C. The prepared electrode was calcined at 300 °C for 1 h before the test, and the thickness of the film was estimated to be ca. 80–120 μm.

### 2.5. DFT calculation

The DFT calculation of  $\text{Bi}_{12}\text{CoO}_{20}$  was performed on Material Studio

with a CASTEP program package [22]. A  $2 \times 1 \times 1$  supercell was used and the model was built similarly according to our published results in  $\text{Bi}_{25}\text{CoO}_{40}$  [21]. The only difference is that in the lattice  $\text{Co}^{3+}$  not only occupies the tetrahedral site but also randomly substitutes at one of the neighbored octahedral sites (Scheme S1, supporting information S1.5). The Generalized Gradient Approximation (GGA) with the parameterization of Perdew–Burke–Ernzerhof (PBE) was used for exchange-correlation functionals. The kinetic energy cutoff was set to 380.0 eV and a Monkhorst-Pack grid with a  $1 \times 2 \times 2$  k-point mesh was used. The geometry optimization convergence thresholds were set with the maximum force of 0.01 eV/Å; maximum stress tolerance of 0.02 GPa; and the maximum atomic displacement of 0.0005 Å. The electronic minimization parameter of the total energy/atom convergence tolerance was  $5.0 \times 10^{-6}$  eV. The calculations were done with designed nonlocal norm-conserving pseudopotentials. For a better description of the d orbitals of transition metal, we also used a Hubbard U parameter for the 3d orbital of Co, which was set to 3 eV as previously reported [23]. For simulating the solar heat-induced  $\text{Co}^{3+}$  to  $\text{Co}^{2+}$  conversion on the charge distribution in the lattice, the  $\text{Co}^{3+}$  cations at octahedral sites ( $\text{Co}_{\text{oct}}$ ) are changed with  $\text{Co}^{2+}$  according to us in-situ XRD, XPS and EPR results. Concurrently, two neighbored octahedral  $\text{Bi}^{3+}$  cations ( $\text{Bi1}_{\text{oct}}$  and  $\text{Bi2}_{\text{oct}}$ ) are changed with  $\text{Bi}^{5+}$  to balance the charge in the lattice.

### 3. Results and discussion

#### 3.1. Controllable preparation of Bi-Co-O series sillenite photocatalysts with different Bi: Co ratios

**Fig. 1(a)** shows XRD patterns of the prepared Bi-Co-O sillenite photocatalysts with different Bi: Co ratios.  $\gamma\text{-Bi}_2\text{O}_3$  was shown as a control as it is the simplest sillenite compound. All the XRD diffraction peaks were assigned to cubic sillenite  $\gamma\text{-Bi}_2\text{O}_3$  (PDF No. 45–1344). No characteristic peaks for impurities ( $\text{CoO}$ ,  $\text{Co}_3\text{O}_4$ ) were observed, indicating that the sillenite photocatalysts were successfully prepared. In particular, the XRD peaks shifted slightly to higher diffraction angles with increasing the Co content. The reason for this phenomenon is the lattice shrinkage caused by the substitution of  $\text{Bi}^{3+}$  (103 pm) with  $\text{Co}^{3+}$  (54.5 pm) [24,

25]. The Co occupation at the tetrahedral sites in the structure has been confirmed by the XRD refinement in our previous work of  $\text{Bi}_{25}\text{CoO}_{40}$  [21]. However, in the  $\text{Bi}_{12}\text{CoO}_{20}$  structure, the content of Co in the lattice was measured as 0.959 by ICP-AES, which is close to the theoretical value (1.00) and higher than our reported  $\text{Bi}_{25}\text{CoO}_{40}$  (0.475). Therefore, the Co content in  $\text{Bi}_{12}\text{CoO}_{20}$  exceeded the theoretical content (0.5) with all the available tetrahedral sites occupied by Co cations, indicating that some Co cations occupy the octahedral sites in the sillenite structure.

**Fig. 1(b)** shows the detailed change of the lattice constants with different Bi: Co ratios. The results show that the lattice constants gradually decreased from 1.0097 nm to 1.0021 nm as the content of Co increased, which is consistent with the XRD peak shift. A maximum 0.753% shrinkage of the lattice constants was observed due to the Co introduction, indicating that Co successfully substitutes Bi in the lattice, as reported in the Co-doped  $\text{Bi}_2\text{O}_3$  and Co-doped  $\text{ZnO}$  systems [26,27].

The Co content to Bi: Co = 6: 1 was also increased further. The XRD pattern of the sample obtained through a similar hydrothermal method is shown in Supporting Information (Fig. S1), and compared with that of  $\text{Bi}_{12}\text{CoO}_{20}$ . The increase of cobalt content disrupted the sillenite structure and some  $\alpha\text{-Bi}_2\text{O}_3$  (PDF No. 65–2366) phases emerged, indicating that the introduction of Co was limited in this example.

**Fig. 1(c)** shows the Raman spectra of the prepared Bi-Co-O sillenite with different Bi: Co ratios. The patterns exhibit peaks located in three regions,  $50\text{--}200\text{ cm}^{-1}$ ,  $200\text{--}600\text{ cm}^{-1}$ , and  $600\text{--}800\text{ cm}^{-1}$ , which were assigned to Bi-O vibrations,  $[\text{BiO}_5\text{E}]$  octahedrons (E denoted as lone electron pairs), and  $[\text{MO}_4]$  tetrahedrons of sillenite, respectively [28]. When the Co content was increased from 0: 100: 1: 25, the Raman spectra remained almost unchanged. However, when the Bi: Co ratio reached 12: 1, the peaks at  $263\text{ cm}^{-1}$  and  $524\text{ cm}^{-1}$  shifted by approximately  $9\text{ cm}^{-1}$  and  $15\text{ cm}^{-1}$ , respectively, to a lower wavenumber relative to those of the samples with other Bi: Co ratios. According to the literature [29], these changes suggest the presence of the large distortion of the octahedral structure in the 12: 1 sample. In our study, the octahedral distortion was likely caused by the substitution of Co with Bi at the octahedral sites.

The SEM image of  $\text{Bi}_{12}\text{CoO}_{20}$  is shown in **Fig. 1(d)**, and the images of

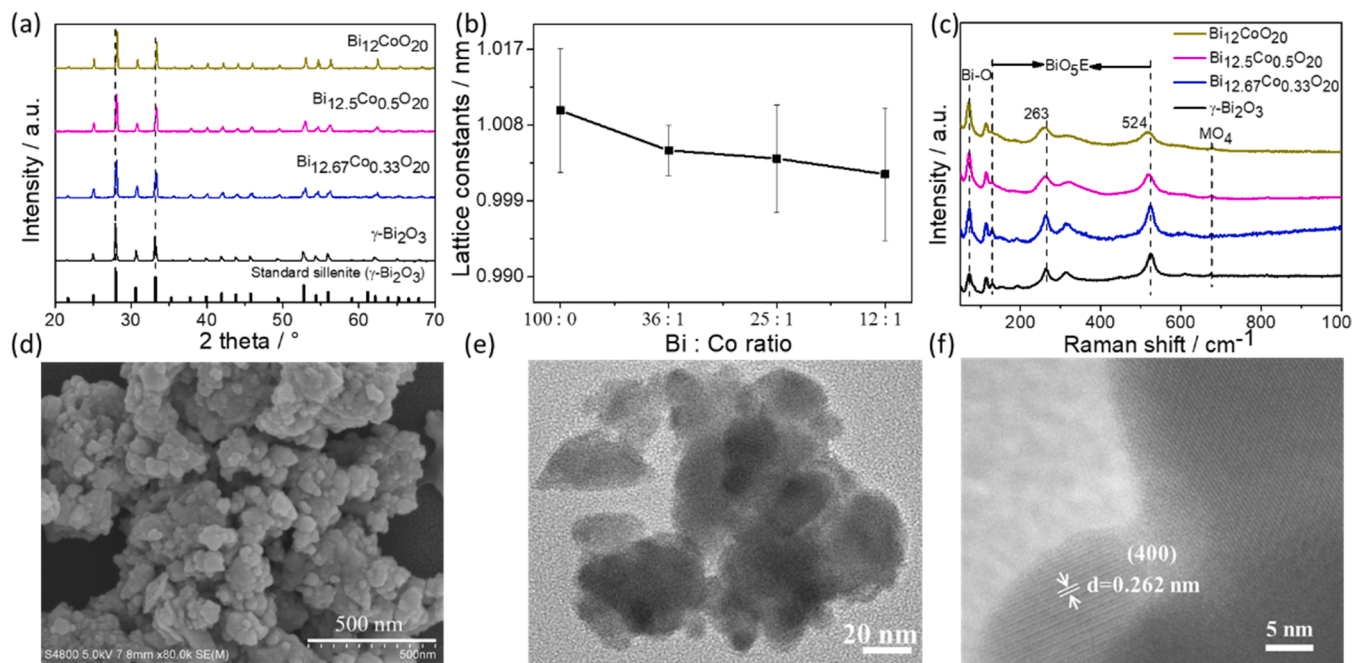


**Fig. 1.** (a) XRD patterns of the prepared Bi-Co-O photocatalysts with different Bi: Co ratios (100: 0, 36: 1, 25: 1, 12: 1); (b) The change of lattice constants with different Bi: Co ratios (100: 0, 36: 1, 25: 1, 12: 1); (c) The Raman spectra of the prepared Bi-Co-O photocatalysts with different Bi: Co ratios (100: 0, 36: 1, 25: 1, 12: 1); SEM (d) and TEM (e and f) images of the prepared  $\text{Bi}_{12}\text{CoO}_{20}$  photocatalyst.

$\text{Bi}_{12.5}\text{Co}_{0.5}\text{O}_{20}$  and  $\text{Bi}_{12.67}\text{Co}_{0.33}\text{O}_{20}$  are shown in Supporting Information (Fig. S2). In the images, the Bi-Co-O series photocatalysts all showed similar morphologies. The photocatalyst exhibited a primary particle size of 80–160 nm, which was twice as large as that of the  $\text{Bi}_{25}\text{Co}_{40}$  [21]. The size was probably due to the increase in hydrothermal temperature and acceleration of the Ostwald ripening process involved in the formation of particles.

Fig. 1(e) shows the TEM image of the  $\text{Bi}_{12}\text{Co}_{20}$  photocatalyst. In the image, the  $\text{Bi}_{12}\text{Co}_{20}$  particles agglomerate, forming larger particle sizes. The lattice image of  $\text{Bi}_{12}\text{Co}_{20}$  is shown in Fig. 1(f). The lattice distance was measured to be 0.262 nm, corresponding to the (400) planes of the sillenite crystal. The BET result of  $\text{Bi}_{12}\text{Co}_{20}$  is shown in Supporting Information (Fig. S3). The sample exhibited a BET surface area of ca.  $0.190 \text{ m}^2 \text{ g}^{-1}$ . The SEM and TEM results show that the prepared  $\text{Bi}_{12}\text{Co}_{20}$  photocatalyst exhibited similar morphological characteristics to our reported  $\text{Bi}_{25}\text{Co}_{40}$  photocatalyst, but the former had a smaller BET surface area due to the increased particle agglomeration resulting from the high hydrothermal temperature.

### 3.2. Excellent photothermal degradation activity of phenols on $\text{Bi}_{12}\text{Co}_{20}$

The photothermal activity of the series photocatalysts was evaluated by the degradation of 5 ppm phenol. Phenol is a typical wastewater pollutant that causes serious diseases at the ppm concentrations.

To investigate the difference in activity of the series photocatalysts (100: 0, 36: 1 and 25: 1) under the photothermal effect, the degradation of phenol on series photocatalysts was measured at different temperatures using an external heat source to control the solution temperature, and the results are shown in Fig. 2(a). The results show that for various Bi: Co ratios (100: 0, 36: 1 and 25: 1), increasing the temperature from 15 °C to 60 °C gradually increased the rate constants (6.1 times at most for the 25: 1 sample), but when Bi: Co = 12: 1, the rate constant was

calculated to be  $0.009 \text{ min}^{-1}$  at 15 °C and  $0.113 \text{ min}^{-1}$  at 60 °C, compromising at a 12.6 times increase. The thermal effect on the performance enhancement of the photocatalyst with a Bi: Co ratio of 12: 1 is the most prominent among all Bi: Co ratios.

Fig. 2(b) shows the activity of  $\text{Bi}_{12}\text{Co}_{20}$  with and without an IR cutoff filter to understand the function of IR light. The suspension preheated to 60 °C with an IR cutoff filter was used as a control. With an IR cutoff filter ( $300 < \lambda < 700 \text{ nm}$ ), the activity decreased largely relative to that without the IR cutoff filter. But when the solution was preheated and maintained at 60 °C during the photodegradation process, the activity with the IR cutoff filter was nearly the same as that without an IR cutoff filter. The results indicate that IR light may be the main heat source that causes the solution temperature increase, while the non-radiative heat generated by charge carrier recombination also contributes to the temperature increases [30], together enhancing the activity.

The in-situ temperature changes of phenol solutions in the presence of  $\text{Bi}_{12}\text{Co}_{20}$  with and without an IR cutoff filter are shown in Fig. 2(c). The temperature change in the presence of  $\gamma\text{-Bi}_2\text{O}_3$  without the IR cutoff filter is shown as a control. The solution temperature of the  $\text{Bi}_{12}\text{Co}_{20}$  without an IR filter rapidly increased from 25 °C to 60 °C within 10 min, while with the IR cutoff filter, the solution temperature increased only to 33 °C. Without the IR filter (control sample), the temperature of the  $\gamma\text{-Bi}_2\text{O}_3$  only reached 38 °C. In the literatures, increasing the temperature to approximately 60 °C by Xe lamp irradiation generally requires 35 min or more for the photothermal degradation of organic pollutants [31,32]. The rapid temperature increase in our study indicates that  $\text{Bi}_{12}\text{Co}_{20}$  exhibits excellent photothermal conversion capability, the origin of which may be derived from its wide-spectrum adsorption with an onset wavelength extending up to the IR region (1000 nm) (Supporting Information, Fig. S4). The extended wavelength and the resulting photothermal effect may be due to the introduction of Co species in the lattice structure, as reported in literatures [8,33]. However, the

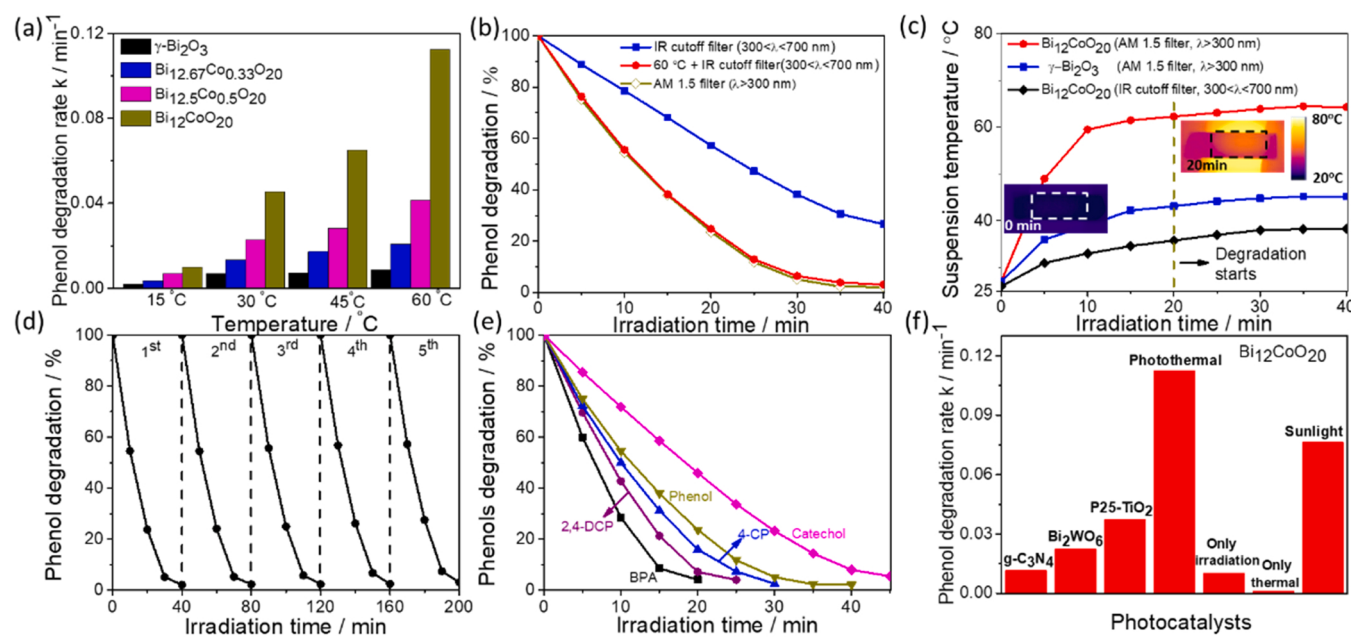


Fig. 2. (a) Photothermal degradation rate of phenol on the prepared Bi-Co-O series photocatalysts at different temperatures (15 °C, 30 °C, 45 °C, 60 °C) controlled by the external heat source. (b) Photothermal degradation of phenol on  $\text{Bi}_{12}\text{Co}_{20}$  photocatalysts with an AM 1.5 filter and with an IR cutoff filter at 60 °C or without temperature control. (c) Temperature changes during the irradiation on  $\text{Bi}_{12}\text{Co}_{20}$  suspension with and without an IR cutoff filter, and on  $\gamma\text{-Bi}_2\text{O}_3$  suspension with the AM 1.5 filter. Dash line is denoted as the starting time point of degradation by adding the model pollutants into the suspension. Inset is the thermal image of  $\text{Bi}_{12}\text{Co}_{20}$  powders (in the dash line box) on glass slides covered with water. (d) Stability of  $\text{Bi}_{12}\text{Co}_{20}$  photocatalysts during the photothermal degradation. (e) Photothermal degradation curves of BPA, 2,4-DCP, 4-CP, catechol and phenol on  $\text{Bi}_{12}\text{Co}_{20}$  with AM 1.5 filter. (f) Photothermal degradation rate constants of phenol on  $\text{Bi}_{12}\text{Co}_{20}$  at different conditions and on P25-TiO<sub>2</sub>,  $\text{g-C}_3\text{N}_4$ , and  $\text{Bi}_2\text{WO}_6$  photocatalysts with the same photothermal conditions. Only thermal (60 °C); Only irradiation (Xe lamp and 25 °C); Sunlight (Wuxi, China (120.27° E, 31.48° N), 12:00 pm to 13:00, July 12, 2021, sunlight intensity,  $90 \text{ mW cm}^{-2}$ , temp: 45–55 °C); Photothermal: a Xe lamp with an AM 1.5 filter without cooling water (suspension temperature for  $\text{Bi}_{12}\text{Co}_{20}$  and for other photocatalysts (P25,  $\text{Bi}_2\text{WO}_6$ , and  $\text{g-C}_3\text{N}_4$ ) stabilized at ca. 60–65 °C and 40–45 °C, respectively). (Cat. 0.5 g/L,  $\text{H}_2\text{O}$  50 ml, phenol 5 ppm).

solution temperature of the  $\text{Bi}_{12}\text{CoO}_{20}$  with the IR cutoff filter slightly changed, confirming that the heat causing the increase in the solution temperature originated from the conversion of IR light. The slight increase in the solution temperature with the IR cutoff filter may have originated from the heat generated from the non-radiative recombination of charge carriers [30] or electron-electron scattering [34]. In all cases, the temperature of the solution reached thermal equilibrium at approximately 20 min, so the pollutants were added at that time to avoid the influence of temperature fluctuation.

The stability test was carried out by carefully collecting the photocatalysts after the reaction by centrifugation, washing with water and ethanol, and drying at 60 °C in an oven for 4 h in air. The collected powders were reused for the next test. The results show that the photothermal activity of phenol degradation did not change after 5 cycles, indicating that  $\text{Bi}_{12}\text{CoO}_{20}$  was stable at elevated temperature and had good photocorrosion resistance. The XRD patterns and Raman spectra of  $\text{Bi}_{12}\text{CoO}_{20}$  before and after the photothermal reaction are shown in Supporting Information (Fig. S5). The results showed that the intrinsic structure of the catalyst was not changed after the photothermal reaction. The stability of the  $\text{Bi}_{12}\text{CoO}_{20}$  photocatalyst is superior to that of the reported photocatalysts containing  $\text{Bi}^{5+}$  or  $\text{Co}^{3+}$  in the structure, such as  $\text{NaBiO}_3$  and  $\text{LaCoO}_3$  [35,36]. The excellent stability may have originated from the band structure of the Bi-Co-O sillenite photocatalyst, which is effective in reducing photocorrosion of the prepared photocatalyst, similar to the reported  $\text{Bi}_{25}\text{CoO}_{40}$  photocatalyst [21].

Concurrent total organic carbon (TOC) removal during the photothermal degradation of phenol on the prepared  $\text{Bi}_{12}\text{CoO}_{20}$  photocatalyst was tested, and the results are shown in Supporting Information (Fig. S6). P25-TiO<sub>2</sub> is listed as a control. The  $\text{Bi}_{12}\text{CoO}_{20}$  photocatalyst achieved approximately 86% TOC removal after 180 min of irradiation. In contrast, TiO<sub>2</sub> exhibited 74% TOC removal over the same period. The high mineralization capability indicates that the photothermal effect not only accelerates degradation but also promotes mineralization.

Next, other typical phenolic pollutants, such as bisphenol A (BPA), 2,4-dichlorophenol (2,4-DCP), 4-chlorophenol (4-CP) and catechol were selected to evaluate the selectivity of photothermal degradation. Fig. 2(e) shows that  $\text{Bi}_{12}\text{CoO}_{20}$  completely degraded BPA, 2,4-DCP, 4-CP, phenol and catechol within 20–45 min, indicating that the high photothermal activity of  $\text{Bi}_{12}\text{CoO}_{20}$  photocatalyst is universal. In literatures, 2,4-DCP and phenol are regarded as pollutants that are difficult to photodegrade, and their complete removal usually takes 3 to more than 5 h [37,38]. In our experiments, these pollutants were removed within just 25 min due to the photothermal effect. The large enhancement suggests that our photocatalyst,  $\text{Bi}_{12}\text{CoO}_{20}$ , is a good candidate for photothermal degradation.

As a comparison, the degradation activity of typical photocatalysts [14,39], such as P25-TiO<sub>2</sub>, g-C<sub>3</sub>N<sub>4</sub> and  $\text{Bi}_2\text{WO}_6$  under the same photothermal conditions is shown in Fig. 2(f). In all cases, sunlight was simulated by Xe lamp irradiation with an AM 1.5 filter, and sunlight heat (photothermal effect) was achieved by irradiation without cooling water. The degradation rate constant of  $\text{Bi}_{12}\text{CoO}_{20}$  was  $0.113 \text{ min}^{-1}$  (TOF ca.  $1.40 \times 10^{-3} \text{ mol (phenol) mol}^{-1} (\text{Bi}_{12}\text{CoO}_{20}) \text{ s}^{-1}$ ) [40], approximately 3.0 times, 10.0 times and 5.1 times higher than those of P25-TiO<sub>2</sub>, g-C<sub>3</sub>N<sub>4</sub> and  $\text{Bi}_2\text{WO}_6$ , respectively. The results show that the prepared  $\text{Bi}_{12}\text{CoO}_{20}$  photocatalyst exhibited photothermal activity that was superior to that of typical photocatalysts. The activity of the prepared photocatalyst,  $\text{Bi}_{12}\text{CoO}_{20}$ , is also at the top level by comparison with other reported IR-responsive photocatalysts, as shown in the Supporting Information (Table S1).

The photothermal activity of phenol degradation on g-C<sub>3</sub>N<sub>4</sub>,  $\text{Bi}_2\text{WO}_6$ , P25-TiO<sub>2</sub> and  $\text{Bi}_{12}\text{CoO}_{20}$  was also tested by a method with the same volumetric rate of photon absorption to exclude the influence of the light-energy-absorption difference on the activity enhancement. The method was carried out according to the reported literature [41], and the results are shown in Supporting Information (Fig. S7). The phenol degradation rates on  $\text{Bi}_2\text{WO}_6$ , g-C<sub>3</sub>N<sub>4</sub> and P25-TiO<sub>2</sub> were  $0.031 \text{ min}^{-1}$ ,

$0.015 \text{ min}^{-1}$  and  $0.057 \text{ min}^{-1}$ , respectively. With the same energy absorption,  $\text{Bi}_{12}\text{CoO}_{20}$  still exhibits 2–7 times higher activity than  $\text{Bi}_2\text{WO}_6$ , g-C<sub>3</sub>N<sub>4</sub> and P25-TiO<sub>2</sub>.

We also evaluated the photoactivity of P25-TiO<sub>2</sub>, g-C<sub>3</sub>N<sub>4</sub> and  $\text{Bi}_2\text{WO}_6$  by preheating the phenol solution to 60 °C (Supporting Information Fig. S8). At 60 °C, the activity of these photocatalysts is still far below (approximately 1/4–1/2) that of the prepared  $\text{Bi}_{12}\text{CoO}_{20}$  photocatalyst, indicating that there are other factors that promote the photocatalytic activity beyond the acceleration of the motion of pollutant molecules originating from the temperature increase.

To better understand the photothermal effect, the degradation of phenol on  $\text{Bi}_{12}\text{CoO}_{20}$  photocatalyst with only irradiation (photo effect) or under the evaluated temperature (thermal effect) and with photothermal synergistic effect is shown in Fig. 2(f). The temperature was controlled at 60 °C in the thermal degradation process, because this was the average temperature naturally reached by the heat from the light source (Xe lamp with an AM 1.5 filter) during photothermal degradation.  $\text{Bi}_{12}\text{CoO}_{20}$  exhibited negligible phenol degradation with only thermal effects, while with only light irradiation, the degradation rate constant was only one tenth of that with photothermal effect ( $0.113 \text{ min}^{-1}$ ). The activity difference indicates that the degradation originates from light excitation, not due to thermal catalysis, and heat can accelerate the reaction.

Inspired by the excellent photothermal activity under simulated sunlight,  $\text{Bi}_{12}\text{CoO}_{20}$  was also evaluated under actual sunlight. As shown in Supporting Information (Fig. S9) and Fig. 2(f), 5 ppm phenol was completely degraded within 45 min under sunlight irradiation, and the degradation rate constant was calculated to be  $0.078 \text{ min}^{-1}$  as shown in Fig. 2(f). The result indicates that  $\text{Bi}_{12}\text{CoO}_{20}$  has excellent performance for potential practical use. The superior photothermal activity of the  $\text{Bi}_{12}\text{CoO}_{20}$  may be derived from the efficient utilization of incident light and the photothermal conversion capability derived from Co species in the structure, as discussed below.

As mentioned in the above discussions of activity, the variation in composition leads to the band adsorption difference and to the activity change. More importantly, the difference between  $\text{Bi}_{12}\text{CoO}_{20}$  and other Bi-Co-O compounds in the series is the occupation of  $\text{Co}^{3+}$  cations at the octahedral sites, as discussed below.

### 3.3. Photothermal enhancement of the photocatalytic activity by promotion of the charge separation and the yield of reactive oxidation species

Transient photocurrent, electrochemical impedance, open circuit potential (OCP) decay and surface photovoltage are used to evaluate the recombination rate in the  $\text{Bi}_{12}\text{CoO}_{20}$  photothermal catalyst. Fig. 3(a) shows the transient photocurrent of the  $\text{Bi}_{12}\text{CoO}_{20}$  photocatalyst at 60 °C (thermal effect), with only irradiation at 25 °C (photo effect), at 60 °C plus irradiation (photothermal effect) and at 60 °C plus irradiation with an IR cutoff filter (cold light plus thermal effect). The current was recorded while the light was switched on and off in intervals of 40 s. No current was observed when the  $\text{Bi}_{12}\text{CoO}_{20}$  photocatalyst received only thermal treatment, while the current reached up to  $3.5 \mu\text{A cm}^{-2}$  under photothermal effect; this current was 3.2 times higher than that under only irradiation ( $1.1 \mu\text{A cm}^{-2}$ ). The increase in the transient photocurrent indicates that the photothermal effect can significantly promote the charge separation efficiency in the  $\text{Bi}_{12}\text{CoO}_{20}$  photocatalyst. At 60 °C and with an IR cutoff filter, only slight photocurrent decrease was observed relative to that without the IR filter but with external heat, indicating that the effect of heat caused by IR light on the photocatalytic reaction is similar to that caused by the external heat source. Therefore, the external heat source was used to control the temperature for all the following measurements instead of a Xe lamp, because the former maintained a more stable temperature than the latter.

Fig. 3(b) shows the electrochemical impedance spectra (EIS) of the  $\text{Bi}_{12}\text{CoO}_{20}$  photocatalyst, these spectra were used to study the

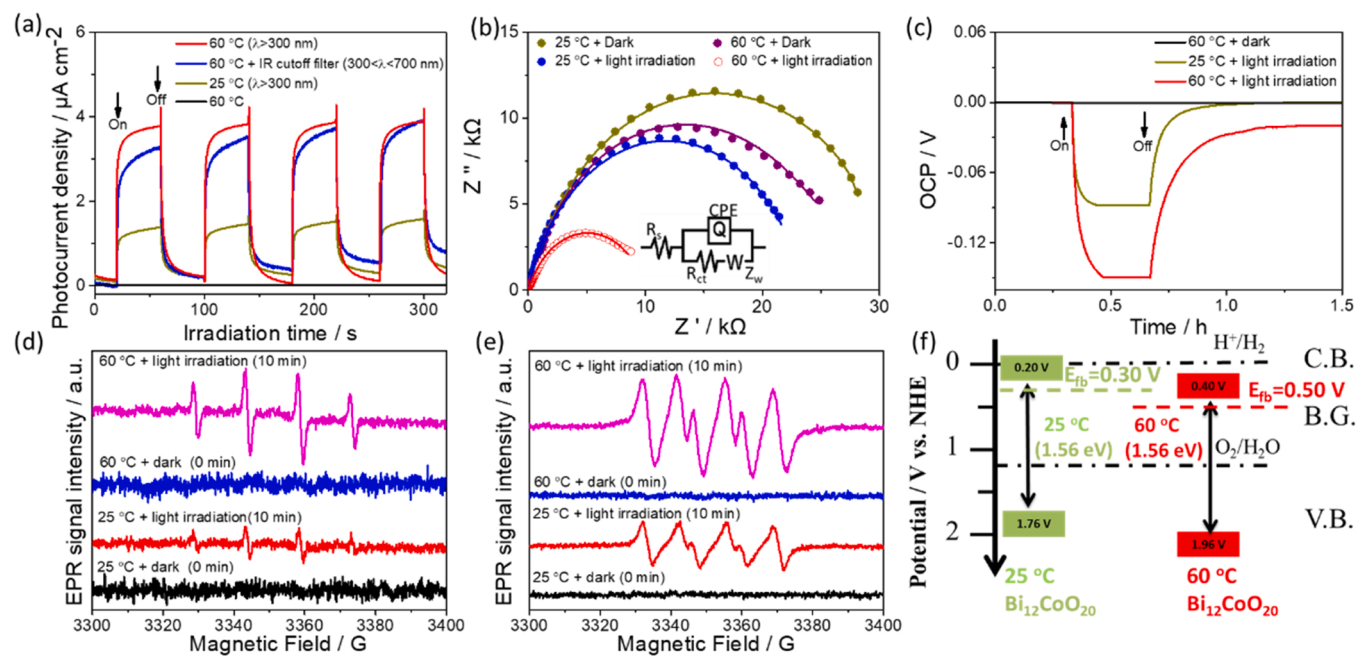


**Fig. 3.** (a) Transient photocurrent for  $\text{Bi}_{12}\text{CoO}_{20}$  with thermal effect (dark +  $60^\circ\text{C}$ ), with only irradiation (Xe lamp), with cold light and thermal effect (Xe lamp with an IR filter +  $60^\circ\text{C}$ ), and with photothermal effect (Xe lamp +  $60^\circ\text{C}$ ); (b) Electrochemical impedance measurements for  $\text{Bi}_{12}\text{CoO}_{20}$  in dark, with thermal effect ( $60^\circ\text{C} + \text{dark}$ ), with only irradiation, and with photothermal effect; (c) Open circuit potential (OCP) decay for  $\text{Bi}_{12}\text{CoO}_{20}$  with thermal effect (dark +  $60^\circ\text{C}$ ), only irradiation, and with photothermal effect; (d-e) EPR spectra of  $\text{Bi}_{12}\text{CoO}_{20}$  under Xe lamp irradiation (AM 1.5 filter) at  $25^\circ\text{C}$  and  $60^\circ\text{C}$ , hydroxyl radicals detection (d) in aqueous with DMPO as a radical trapper, superoxide radicals detection (e) in methanol with DMPO as a radical trapper; and (f) Band edge positions (versus NHE, pH=0) of  $\text{Bi}_{12}\text{CoO}_{20}$  at  $25^\circ\text{C}$  and  $60^\circ\text{C}$ .

photothermal effect. The spectra were obtained at  $25^\circ\text{C}$  and  $60^\circ\text{C}$  in the dark and at  $25^\circ\text{C}$  and  $60^\circ\text{C}$  with Xe lamp irradiation, respectively. The inset in Fig. 3(b) shows the Randles circuit used to simulate the impedance results, as this circuit has been verified in other semiconductor systems [42].  $\text{Bi}_{12}\text{CoO}_{20}$  exhibits similar semicircles under above the conditions but with different radii. The small radius suggests the low resistance of charge transfer. In the  $\text{Bi}_{12}\text{CoO}_{20}$  photocatalyst,  $R_{ct}$ , a sign of charge transfer, was approximately  $31.8 \text{ k}\Omega$ ,  $24.3 \text{ k}\Omega$ ,  $23.2 \text{ k}\Omega$ , and  $10.1 \text{ k}\Omega$  (detailed in the Supporting Information Table S2) under the above conditions. To exclude the increase in conductivity of  $\text{Bi}_{12}\text{CoO}_{20}$  due to increasing temperature, the dark- $R_{ct}$  at different temperatures was set as a baseline. The ratio of the difference between the  $R_{ct}$ -light on and  $R_{ct}$ -dark at  $25^\circ\text{C}$  and  $60^\circ\text{C}$  to the  $R_{ct}$ -dark was used to express the decrease in  $R_{ct}$  due to irradiation at  $25^\circ\text{C}$  and  $60^\circ\text{C}$ . The difference in  $R_{ct}$  was  $8.6 \text{ k}\Omega$ , and the ratio was 0.27 at  $25^\circ\text{C}$ . While the difference in  $R_{ct}$  was  $14.2 \text{ k}\Omega$ , and the ratio was 0.58 at  $60^\circ\text{C}$ . Thus, the decrease in  $R_{ct}$ -light on at  $60^\circ\text{C}$  was 2.1 times higher than that at  $25^\circ\text{C}$ , indicating that the charge separation was enhanced by the thermal effect. Therefore, the photothermal effect significantly facilitates  $\text{Bi}_{12}\text{CoO}_{20}$  charge separation and transfer.

The open circuit potential (OCP) decay of  $\text{Bi}_{12}\text{CoO}_{20}$  with photo effect (at  $25^\circ\text{C}$  with irradiation), photothermal effect (at  $60^\circ\text{C}$  with irradiation) and thermal effect (at  $60^\circ\text{C}$  without irradiation) is shown in Fig. 3(c). The decay of OCP is caused by the recombination of photogenerated electron-hole pairs. Thus, faster OCP decay means faster recombination of photogenerated electron-hole pairs. During the experiments, the sample was first maintained at  $60^\circ\text{C}$  or  $25^\circ\text{C}$  under irradiation and then left in the dark to release OCP. First, no change in the OCP was observed for  $\text{Bi}_{12}\text{CoO}_{20}$  at  $60^\circ\text{C}$  in the dark, indicating that the thermal effect cannot initiate  $e^-$  and  $h^+$  separation. In contrast, the OCP with the photothermal effect reached  $-0.15 \text{ V}$ , much higher than that under only irradiation ( $-0.10 \text{ V}$ ). The kinetic constants of the decay process were obtained by exponential regression fitting [43] and were determined to be  $1.71 \times 10^{-4} \text{ s}^{-1}$  and  $7.97 \times 10^{-3} \text{ s}^{-1}$  for the sample with the photothermal effect and that with only irradiation,

respectively. The smaller kinetic constant and higher OCP indicate that the charge separation efficiency of the  $\text{Bi}_{12}\text{CoO}_{20}$  photocatalyst was enhanced by the photothermal effect.

The surface photovoltage (SPV) of the  $\text{Bi}_{12}\text{CoO}_{20}$  photocatalyst under only irradiation and with photothermal effect is shown in Supporting Information (Fig. S12). In both cases, the photovoltage responses ranged from 300 nm to 800 nm, consistent with the UV-DRS spectra. This result confirms that the photothermal activity of phenol degradation was derived from band excitation. In particular, the photovoltage with the photothermal effect was higher than that under irradiation alone. According to the literature [44], the surface photovoltage originates from the separation of photogenerated electron-hole pairs, where a higher SPV response indicates a better photogenerated charge separation efficiency.

The ex-situ PL and PL decay spectra of the  $\text{Bi}_{12}\text{CoO}_{20}$  photocatalyst at  $25^\circ\text{C}$  and  $60^\circ\text{C}$ , respectively, are shown in Supporting Information (Fig. S13). In Fig. S13 (a), the PL peak intensity of the  $\text{Bi}_{12}\text{CoO}_{20}$  photocatalyst at  $25^\circ\text{C}$  is twice as high as that at  $60^\circ\text{C}$ , indicating that the thermal effect can suppress the recombination of photogenerated carriers. The emission peak at 468 nm is derived from excitation at 350 nm, which corresponds to excitation from the O 2p to the Bi 6p orbitals of  $\text{Bi}_{12}\text{CoO}_{20}$ . The PL decay spectra were measured at  $25^\circ\text{C}$  and elevated temperature (approximately  $60^\circ\text{C}$ ) on a fluorescence lifetime spectrometer (Lifespec II, Edinburgh). A pulse laser (EPL375) was used in the measurements. The time-correlated single photon counting (TCSPC) method was used to record the results. The software (F980) equipped in the instrument was used to fit the PL decay curves, and the detailed fitting equation is given in Supporting Information (S1.3). In Fig. S13 (b), the decay time for the  $\text{Bi}_{12}\text{CoO}_{20}$  photocatalyst at  $60^\circ\text{C}$  is approximately 4.19 ns, and that at  $25^\circ\text{C}$  is 3.47 ns (detailed fitting parameters are listed in Table S3 of the Supporting Information). The decay time is also derived from a deeper energy band excitation process, as the transition from the O 2p to Bi 6p orbitals in the  $\text{Bi}_{12}\text{CoO}_{20}$  structure. The longer lifetime of photogenerated carriers indicates that the thermal effect can slow the recombination rate in the  $\text{Bi}_{12}\text{CoO}_{20}$  photocatalyst.

Next, the reactive oxygen species (ROS) with and without photo-thermal effect were detected. Hydroxyl radicals ( $\cdot\text{OH}$ ), superoxide radicals ( $\cdot\text{O}_2^-$ ) and holes ( $\text{h}^+$ ) can be generated during photocatalysis and initiate photothermal degradation [45]. The EPR results are shown in Fig. 3(d) and (e) and indicate the detection of the radicals. At 25 °C and 60 °C, there were no obvious peaks corresponding to hydroxyl radicals or superoxide radicals in dark. After 10 min of irradiation, weak signals corresponding to hydroxyl radicals appeared, indicating a considerable number of superoxide radicals, at 25 °C. In contrast, at 60 °C, EPR signals corresponding to hydroxyl radicals and superoxide radicals that had

intensities that were approximately 4- and 2-times higher, respectively, than those at 25 °C were observed. The results indicate that the photo-thermal effect can significantly enhance the generation of ROS. The increase in hydroxyl radicals may originate from the change in the band structure caused by the photo-thermal effect, while the increase in superoxide radicals may be due to the acceleration of  $\text{O}_2$  diffusion to the surface of the photocatalyst (diffusion coefficient:  $1.96 \times 10^{-5} \text{ cm}^2 \text{ s}^{-1}$  at 25 °C and  $4.03 \times 10^{-5} \text{ cm}^2 \text{ s}^{-1}$  at 60 °C) [46].

The ROS trapping experiments are shown in Supporting Information (Fig. S14). Hydroxyl radicals, superoxide radicals and holes can be

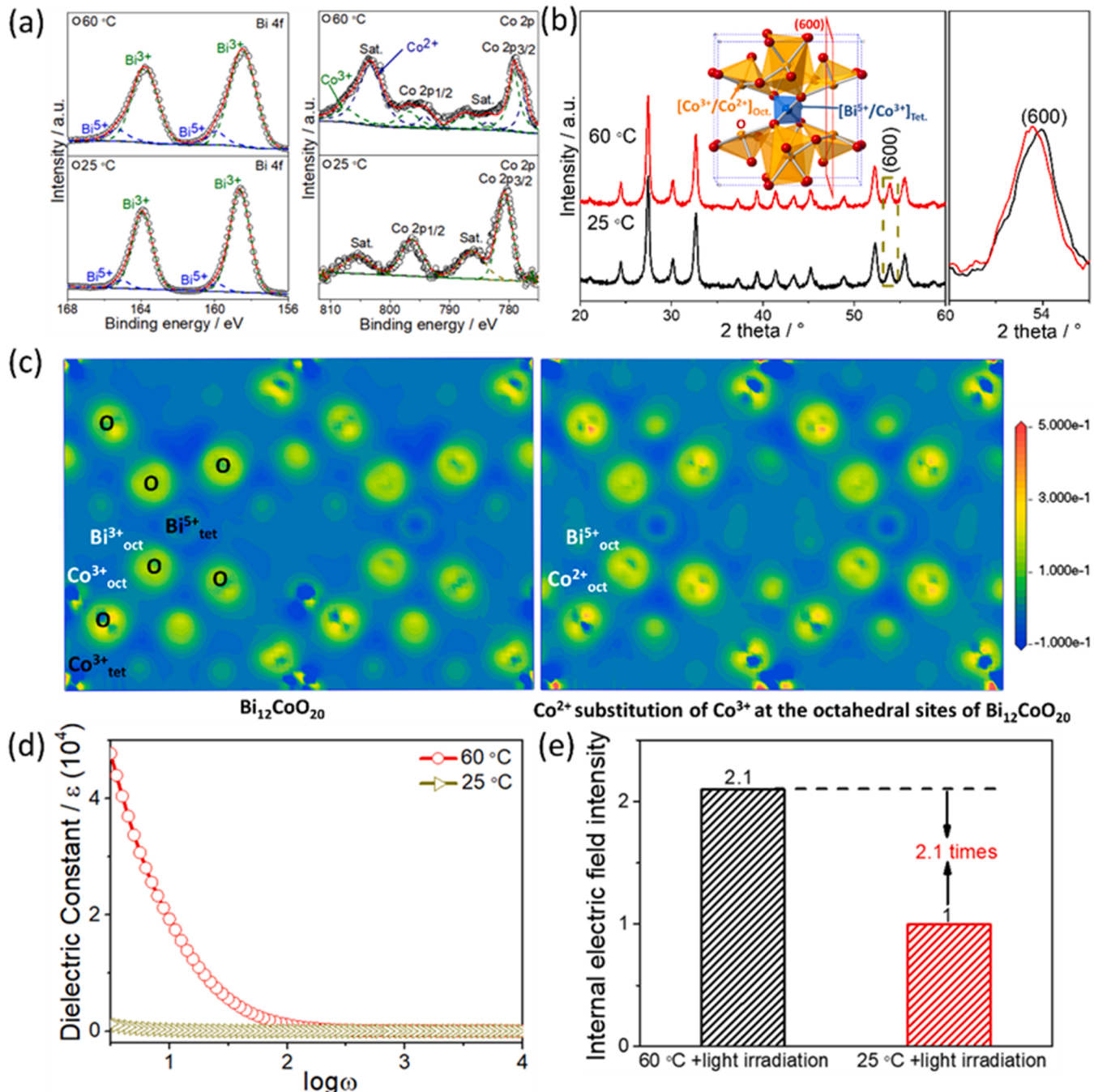


**Fig. 4.** (a) In-situ XPS spectra of  $\text{Bi}_{12}\text{CoO}_{20}$  at 25 °C and 60 °C: Bi 4f and Co 2p; (b) In-situ XRD patterns of  $\text{Bi}_{12}\text{CoO}_{20}$  at 25 °C and 60 °C, and enlarged patterns of (600) peak (Inset is the (600) planes in the lattice); (c) DFT calculated projection of electron density difference on the (011) plane of  $\text{Bi}_{12}\text{CoO}_{20}$  and  $\text{Bi}_{12}\text{CoO}_{20}$  with  $\text{Co}^{2+}$  substitution of  $\text{Co}^{3+}$  at the octahedral sites. tet and oct are denoted as the cations occupying the tetrahedral and octahedral sites in the sillenite structure, respectively; (d) The curves of the dielectric constant of  $\text{Bi}_{12}\text{CoO}_{20}$  against  $\log\omega$  at 25 °C and 60 °C; (e) The internal electric field intensity of  $\text{Bi}_{12}\text{CoO}_{20}$  at 25 °C and 60 °C (assuming the intensity of  $\text{Bi}_{12}\text{CoO}_{20}$  at 25 °C is "1").

trapped by tert-butyl alcohol (t-BuOH), benzoquinone (BQ) and potassium iodide (KI), respectively. The activity of phenol degradation at 25 °C and 60 °C decreased after trapping reagents were added. The addition of KI had a more significant effect on the decrease in the activity than the addition of t-BuOH and BQ in both cases. The results suggest that the holes generated on the Bi<sub>12</sub>CoO<sub>20</sub> photocatalyst play a major role in the phenol degradation process. According to the above results, at 25 °C, only holes degrade phenol, while at 60 °C, holes, hydroxyl radicals and superoxide radicals degrade phenol. The latter clearly exhibits higher activity relative to the former case.

Fig. 3(f) shows the band edge positions for the Bi<sub>12</sub>CoO<sub>20</sub> photocatalyst, which are determined by flat band potential measurements [47] and bandgap. The bandgap and flat band potential were measured at 25 °C and 60 °C, respectively, and the results are shown in Supporting Information (Fig. S15). The bandgap measured at 25 °C and 60 °C were both approximately 1.56 eV. The measured flat band potentials of the Bi<sub>12</sub>CoO<sub>20</sub> photocatalyst at 25 °C and 60 °C were 0.087 and 0.293 V vs. Ag/AgCl, respectively. Therefore, the conduction band (CB) and valence band (VB) edge potentials of the Bi<sub>12</sub>CoO<sub>20</sub> photocatalyst were determined to be 0.20 V and 1.76 V at 25 °C, and 0.40 V and 1.96 V at 60 °C, respectively. The change of the band edge potentials at 60 °C may be due to the change of band structure originating from the change of the valence state of Co in the lattice (detailed in Section 3.4).

The HPLC spectra of the photothermal degradation of phenol is shown in Supporting Information (Fig. S16). In the figure, the peak of phenol rapidly decreased with 30 min irradiation due to the photothermal effect. Benzoquinone (BQ) and hydroquinone (HQ) were found to be the key intermediates during phenol degradation, similar to many literatures reported that studied only photocatalytic phenol degradation [48,49]. The similar degradation behavior with and without the thermal effect indicates that the photothermal effect does not influence the degradation pathway.

### 3.4. The enhancement of charge transfers and ROS generation originating from the thermally induced Co<sup>3+</sup> to Co<sup>2+</sup> conversion at the octahedral sites of sillenite and the relevant promotion of the lattice dipole and internal electric field

According to the above results, the photothermal effect was found to accelerate the charge separation and the generation of ROS, leading to the enhancement of the degradation of phenols. The reasons for the actions of the photothermal effect will be discussed below.

Fig. 4(a) shows in-situ XPS measurements to clarify the valence state change of Bi and Co in the Bi<sub>12</sub>CoO<sub>20</sub> lattice at 25 °C and 60 °C, respectively. The Bi 4 f XPS scan exhibits two pairs of peaks. They are located at around 163.9–158.6 eV and 165.1–159.8 eV, respectively, which can be assigned as Bi<sup>3+</sup> and Bi<sup>5+</sup> according to the literature [25]. At 25 °C, the ratio of Bi<sup>5+</sup>: Bi<sup>3+</sup> is 6.6%: 93.4%, while at 60 °C, the ratio increases to 14.4%: 85.6%, indicating the Bi<sup>5+</sup> content increases with increasing the temperature.

Similarly, the Co 2p XPS scan exhibits a valence state change with increasing temperature. At 25 °C, two pairs of peaks can be observed, with one pair of main peaks located at around 795.8 and 780.3 eV, and one pair of satellite peaks located at around 805.5 and 785.7 eV, respectively. The main and satellite peaks are assigned as Co<sup>3+</sup> 2p<sub>1/2</sub> and 2p<sub>3/2</sub>, according to the literature (Fig. 4(a)) [50]. When increasing the temperature, two pairs of new peaks can be observed, with one pair of main peaks located at around 794.2 and 778.5 eV, and the other pair of satellite peaks at 803.5 and 782.9 eV. These peaks correspond to the presence of Co<sup>2+</sup> according to the literature [51]. The satellite peaks of Co<sup>2+</sup> are stronger than the main peak, indicating that Co<sup>2+</sup> emerges at the octahedral sites of sillenite at elevated temperature. In previous reports on CoO and Co<sub>3</sub>O<sub>4</sub>, similar Co XPS spectra are observed and considered to originate from the high overlap of Co 2p and O 2p orbitals in distorted [CoO<sub>6</sub>] octahedrons [52]. In our study, sillenite exhibits a high degree of distortion for its octahedral sites (BiO<sub>5</sub>E), and Co species

partially occupy those sites, as observed in Fig. 1(c). Therefore, the nature of the sillenite structure may lead to the formation of highly distorted Co<sup>3+</sup> octahedrons. Since Co<sup>3+</sup> has no lone electron pairs, as does Bi<sup>3+</sup>, the octahedral structure of the occupied Co<sup>3+</sup> may only need to overcome a small energy barrier, so it can use solar heat to accept e<sup>-</sup>, forming Co<sup>2+</sup>, and the amount of Co<sup>3+</sup> converted at evaluated temperature is 0.137 relative to the unchanged Co<sup>3+</sup>.

According to the XPS spectra, the temperature increase results in the formation of Co<sup>2+</sup> at octahedral sites and Bi<sup>5+</sup>. According to our previous study and the above discussions [21], the molecular formula of Bi<sub>25</sub>CoO<sub>40</sub> should be Bi<sub>24</sub><sup>III</sup>(Bi<sup>V</sup> Co<sup>III</sup>)O<sub>40</sub>, while that of the prepared Bi<sub>12</sub>CoO<sub>20</sub> should be (Bi<sub>11.5</sub><sup>III</sup> Co<sub>0.5</sub><sup>III</sup>) (Bi<sub>0.5</sub><sup>V</sup> Co<sub>0.5</sub><sup>III</sup>)O<sub>20</sub>. Therefore, in the Bi<sub>12</sub>CoO<sub>20</sub> lattice, no Bi<sup>3+</sup> cations remain at the tetrahedral sites, and the Bi<sup>5+</sup> formed by the thermal effect must occupy the octahedral sites. To minimize the formation energy of Co<sup>2+</sup> and Bi<sup>5+</sup> cations both at octahedral sites, these cations may form at neighboring sites by transferring electrons from Bi<sup>3+</sup> to adjacent Co<sup>3+</sup> in the original sillenite.

The in-situ XRD patterns of Bi<sub>12</sub>CoO<sub>20</sub> at 25 °C and 60 °C are shown in Fig. 4(b). They show that there are no impurities at 60 °C, indicating that the structure of Bi<sub>12</sub>CoO<sub>20</sub> is stable at this temperature. In the enlarged patterns, the (600) peaks shift to a lower diffraction angle (approximately 0.093°) at 60 °C relative to that at 25 °C, while other peaks remain almost unchanged (Supporting Information, Fig. S17). The (600) planes are mainly composed of Co<sup>3+</sup> and Bi<sup>3+</sup> cations at the octahedral sites (Fig. 4(b) inset). Therefore, the low angle shifts of the (600) planes indicate an increase in the ionic radii of Co cations. The radius increase may be due to the heat-induced conversion of Co<sup>3+</sup> (54.5 pm) to Co<sup>2+</sup> (72 pm) at 60 °C [24,53].

The in-situ EPR measurement further confirmed the conversion of Co<sup>3+</sup> to Co<sup>2+</sup> at 60 °C, as shown in the Supporting Information (Fig. S18). The g value of the Co EPR peaks changes from 2.007 at 25 °C to 2.018 at 60 °C, indicating that the valence state of Co changed from +3 to +2 in Bi<sub>12</sub>CoO<sub>20</sub> according to the reported literature [54].

The in-situ XPS, XRD and EPR results all demonstrate that heat can cause the conversion of octahedral Co<sup>3+</sup> to Co<sup>2+</sup> in the Bi<sub>12</sub>CoO<sub>20</sub> structure. In other Co compounds, such as Co<sub>3</sub>[Fe(CN)<sub>6</sub>]<sub>2</sub>·xH<sub>2</sub>O and Na<sub>x</sub>CoyFe(CN)<sub>6</sub>·zH<sub>2</sub>O, the conversion of Co<sup>3+</sup> to Co<sup>2+</sup> at elevated temperature (approximately 80 °C) has also been observed [55,56]. We also evaluated the XRD pattern of Bi<sub>12</sub>CoO<sub>20</sub> after the reaction (Supporting Information, Fig. S5), and no such (600) peak shift was observed, indicating that the conversion of Co<sup>3+</sup> to Co<sup>2+</sup> at elevated temperature is reversible.

In the reported Bi<sub>25</sub>CoO<sub>40</sub>, the 3d orbitals of Co mainly contribute to the valence band according to previous DFT calculations [21]. In the present Bi<sub>12</sub>CoO<sub>20</sub> structure, when the Co<sup>3+</sup> at the octahedral sites changes to Co<sup>2+</sup>, the Co 3d orbitals contribute more to the conduction band and decrease its contribution to the valence band maximum, resulting in the more positive valence band maximum, closer to that of the Bi 6 s-O 2p orbitals (approximately 2.8 eV obtained from Bi<sub>2</sub>O<sub>3</sub>). Therefore, the change in the valence state of Co caused by the photothermal effect may be responsible for the observed band position change and the increased yield of ROS shown in Fig. 3(d-f). In the reported Co-based photocatalysts [57,58], a similar tendency was also reported to lead to a more positive valence band maximum of CoO relative to that of Co<sub>3</sub>O<sub>4</sub>.

The projection of the electron density difference on the (011) planes calculated by DFT methods is shown in Fig. 4(c) to further clarify the influence of the photothermal change of octahedral Co<sup>3+</sup> to Co<sup>2+</sup>. Neighboring Bi<sup>3+</sup> and Co<sup>3+</sup> cations at the octahedral sites were substituted with Bi<sup>5+</sup> and Co<sup>2+</sup> to simulate the influence of heat-induced Co<sup>3+</sup> to Co<sup>2+</sup> conversion on the charge distribution of the sample (detailed in 2.5, DFT calculation). In the figure, the difference in the charge distribution of Co<sub>3</sub><sup>3+</sup> and Bi<sub>tet</sub><sup>5+</sup> at the tetrahedral sites remained consistent, similar to what we observed in Bi<sub>25</sub>CoO<sub>40</sub>, indicating that heat does not influence the charge distribution at the tetrahedral sites. At the octahedral sites, the difference in charge distribution between

neighboring  $\text{Bi}^{3+}$  and  $\text{Co}^{3+}$  is small, while the difference becomes distinct after the substitution of  $\text{Bi}^{5+}$  and  $\text{Co}^{2+}$ . The different charge distributions indicate that the formation of  $\text{Bi}^{5+}$  and  $\text{Co}^{2+}$  at the octahedral sites by the photothermal effect forms a dipole in the lattice.

The increase in the lattice dipole can be reflected by dielectric constant measurements at 25 °C and 60 °C (Fig. 4(d)). Generally, materials with large dipoles have high dielectric constants [59]. In our case, the dielectric constant at 60 °C is clearly larger than that at 25 °C, indicating that the dipole moment increases with increasing temperature.

We also evaluated the internal electric field at 25 °C and 60 °C (Fig. 4(e)). It is known that the internal electric field is proportional to the square root of the product of surface voltage and surface charge density [60,61] (Supporting Information S1.6). The former can be measured by the open circuit potential (OCP), while the latter can be obtained from the transient photocurrent [62,63]. In our case, the OCP are measured to be  $-0.10\text{ V}$  at 25 °C and  $-0.15\text{ V}$  at 60 °C (Fig. 3(c)). The surface charge density at 25 °C and 60 °C were measured to be  $0.29\text{ }\mu\text{C cm}^{-2}$  and  $0.83\text{ }\mu\text{C cm}^{-2}$ , respectively, according to the transient photocurrent (Supporting Information Fig. S19). The surface charge density can also be reflected by the zeta-potential measurement. The zeta-potential of  $\text{Bi}_{12}\text{CoO}_{20}$  at 25 °C and 60 °C were determined to be  $-3.12\text{ mV}$  and  $-8.81\text{ mV}$ , respectively, suggesting that the surface charge density obtained at 60 °C was higher than that at 25 °C, consistent with the transient photocurrent results. According to the above, the internal electric field at 60 °C was found to be approximately 2.1 times higher than that at 25 °C.

In our previous work, the high activity of the  $\text{Bi}_{25}\text{CoO}_{40}$  sillenite photocatalyst was due to the formation of a large dipole moment (30.1 D) between  $\text{Bi}^{5+}$  and  $\text{Co}^{3+}$  at the tetrahedral sites. In the case of  $\text{Bi}_{12}\text{CoO}_{20}$ , the formation of neighboring  $\text{Bi}^{5+}$  and  $\text{Co}^{2+}$  at the octahedral sites creates another photothermal induced dipole. The photothermally induced dipole was calculated to be 34.6 D (Supporting Information S1.8), which is compatible with the inherent dipole (30.1 D), as we reported for  $\text{Bi}_{25}\text{CoO}_{40}$  sillenite [21]. The lattice dipole increase doubles the internal electric field and thus improves the charge separation and transfer, leading to excellent photothermal degradation activity.

#### 4. Conclusion

In summary,  $\text{Bi}_{12}\text{CoO}_{20}$ , a new sillenite photocatalyst with wide spectrum adsorption (up to 1000 nm), has been successfully prepared by the hydrothermal method.  $\text{Bi}_{12}\text{CoO}_{20}$  shows superior photothermal activity for the degradation of phenols, 2–8 times higher than those of reported  $\text{Bi}_{25}\text{CoO}_{40}$ ,  $\text{P}25\text{-TiO}_2$ ,  $\text{g-C}_3\text{N}_4$  and  $\text{Bi}_2\text{WO}_6$ . The photothermal effect is demonstrated to lead to the conversion of  $\text{Co}^{3+}$  and  $\text{Bi}^{3+}$  at octahedral sites to  $\text{Co}^{2+}$  and  $\text{Bi}^{5+}$ , resulting in a new photothermally induced dipole. The photothermally induced dipole was found to enhance the internal electric field, promote charge separation, and give  $\text{Bi}_{12}\text{CoO}_{20}$  excellent activity. The enhancement of lattice dipole and internal electric field via the photothermal effect has been established as a novel and effective method of enhancing the activity of wide-spectrum-responsive photocatalysts, and can provide some guidelines for the development of new photocatalytic systems that can efficiently utilize solar energy.

#### CRediT authorship contribution statement

**Zhenlin Wang:** Conceptualization, Methodology, Writing – original draft. **Yanying Wang:** Investigation. **Yanping Zhang:** Validation, Investigation. **Xue Sun:** Investigation. **Yang Lou:** Visualization, Investigation. **Ying Zhang:** Methodology, Formal analysis. **Yuming Dong:** Revision, Resources. **Yongfa Zhu:** Writing – review & editing, Supervision. **Chengsi Pan:** Calculation, Methodology, Writing – review & editing, Supervision.

#### Declaration of Competing Interest

The authors declare that they have no known competing financial interests or personal relationships that could have appeared to influence the work reported in this paper.

#### Acknowledgments

This work was supported by the National Natural Science Foundation of China (22172065, 21908079, 21676123, 21902009, 21707052), Natural Science Foundation of Jiangsu Province (BK20201345), Startup Funding at Jiangnan University (1045210322190170, 1045281602190010, 1042050205204100, 1045219039200010, 1045219032210020), the State Key Laboratory of Fine Chemicals, Dalian University of Technology (KF2005), Fundamental Research Funds for the Central Universities (JUSRP52004B, JUSRP12033), Jiangsu Agriculture Science and Technology Innovation Fund (CX(20)3108).

#### Appendix A. Supporting information

Supplementary data associated with this article can be found in the online version at doi:10.1016/j.apcatb.2022.121452.

#### References

- [1] H. Lu, Q. Hao, T. Chen, L. Zhang, D. Chen, C. Ma, W. Yao, Y. Zhu, A high-performance  $\text{Bi}_2\text{O}_3/\text{Bi}_2\text{SiO}_5$  p-n heterojunction photocatalyst induced by phase transition of  $\text{Bi}_2\text{O}_3$ , *Appl. Catal. B Environ.* 237 (2018) 59–67.
- [2] L. Zhu, M. Gao, C.K.N. Peh, G.W. Ho, Solar-driven photothermal nanostructured materials designs and prerequisites for evaporation and catalysis applications, *Mater. Horiz.* 5 (2018) 323–343.
- [3] E. Yu, J. Li, J. Chen, J. Chen, Z. Hong, H. Jia, Enhanced photothermal catalytic degradation of toluene by loading Pt nanoparticles on manganese oxide: photoactivation of lattice oxygen, *J. Hazard. Mater.* 388 (2020), 121800.
- [4] C. Xu, H. He, Z. Xu, C. Qi, S. Li, L. Ma, P. Qiu, S. Yang, Modification of graphitic carbon nitride by elemental boron cocatalyst with high-efficient charge transfer and photothermal conversion, *Chem. Eng. J.* 417 (2021), 129203.
- [5] L. Wei, C. Yu, K. Yang, Q. Fan, H. Ji, Recent advances in VOCs and CO removal via photothermal synergistic catalysis, *Chin. J. Catal.* 42 (2021) 1078–1095.
- [6] X. Xie, Y. Li, Y. Yang, C. Chen, Q. Zhang, UV-Vis-IR driven thermocatalytic activity of  $\text{OMS-2/SnO}_2$  nanocomposite significantly enhanced by novel photoactivation and synergistic photocatalysis-thermocatalysis, *Appl. Surf. Sci.* 462 (2018) 590–597.
- [7] M. Zhao, T. Chen, B. He, X. Hu, J. Huang, P. Yi, Y. Wang, Y. Chen, Z. Li, X. Liu, Photothermal effect-enhanced photoelectrochemical water splitting of a  $\text{BiVO}_4$  photoanode modified with dual-functional polyaniline, *J. Mater. Chem. A* 8 (2020) 15976–15983.
- [8] S. Xia, Z. Zhang, J. Wu, Y. Wang, M. Sun, Y. Cui, C. Zhao, J. Zhong, W. Cao, H. Wang, M. Zhang, Y. Zheng, X. Li, Cobalt carbide nanosheets as effective catalysts toward photothermal degradation of mustard-gas simulants under solar light, *Appl. Catal. B Environ.* 284 (2021), 119703.
- [9] T. Zhao, Z. Xing, Z. Xiu, Z. Li, P. Chen, Q. Zhu, W. Zhou, Synergistic effect of surface plasmon resonance,  $\text{Ti}^{3+}$  and oxygen vacancy defects on  $\text{Ag}/\text{MoS}_2/\text{TiO}_{2-x}$  ternary heterojunctions with enhancing photothermal catalysis for low-temperature wastewater degradation, *J. Hazard. Mater.* 364 (2019) 117–124.
- [10] G.I. Makhatadze, P.L. Privalov, Partial specific heat capacity of benzene and of toluene in aqueous solution determined calorimetrically for a broad temperature range, *J. Chem. Thermodyn.* 20 (1988) 405–412.
- [11] Y. Huang, Y. Lu, Y. Lin, Y. Mao, G. Ouyang, H. Liu, S. Zhang, Y. Tong, Cerium-based hybrid nanorods for synergistic photo-thermocatalytic degradation of organic pollutants, *J. Mater. Chem. A* 6 (2018) 24740–24747.
- [12] Z. Gan, X. Wu, M. Meng, X. Zhu, L. Yang, P.K. Chu, Photothermal contribution to enhanced photocatalytic performance of graphene-based nanocomposites, *ACS Nano* 8 (2014) 9304–9310.
- [13] H. Fu, L. Zhang, W. Yao, Y. Zhu, Photocatalytic properties of nanosized  $\text{Bi}_2\text{WO}_6$  catalysts synthesized via a hydrothermal process, *Appl. Catal. B Environ.* 66 (2006) 100–110.
- [14] C. Pan, J. Xu, Y. Wang, D. Li, Y. Zhu, Dramatic activity of  $\text{C}_3\text{N}_4/\text{BiPO}_4$  photocatalyst with core/shell structure formed by self-assembly, *Adv. Funct. Mater.* 22 (2012) 1518–1524.
- [15] Y. Guo, W. Shi, Y. Zhu, Y. Xu, F. Cui, Enhanced photoactivity and oxidizing ability simultaneously via internal electric field and valence band position by crystal structure of bismuth oxyiodide, *Appl. Catal. B Environ.* 262 (2020), 118262.
- [16] L. Zhang, Y. Li, Q. Li, J. Fan, S.A.C. Carabineiro, K. Lv, Recent advances on bismuth-based photocatalysts: strategies and mechanisms, *Chem. Eng. J.* 419 (2021), 129484.

[17] Z. Zhang, W. Wang, L. Wang, S. Sun, Enhancement of visible-light photocatalysis by coupling with narrow-band-gap semiconductor: a case study on  $\text{Bi}_2\text{S}_3/\text{Bi}_2\text{WO}_6$ , *ACS Appl. Mater. Interfaces* 4 (2012) 593–597.

[18] M. Wang, J. Gao, G. Zhu, N. Li, R. Zhu, X. Wei, P. Liu, Q. Guo, One-step solvothermal synthesis of Fe-doped BiOI film with enhanced photocatalytic performance, *RSC Adv.* 6 (2016) 106615–106624.

[19] Y. Zheng, W. Wang, D. Jiang, L. Zhang, Amorphous MnO<sub>x</sub> modified Co<sub>3</sub>O<sub>4</sub> for formaldehyde oxidation: improved low-temperature catalytic and photothermocatalytic activity, *Chem. Eng. J.* 284 (2016) 21–27.

[20] H. Liu, Y. Zhang, X. Zhang, H. Chen, R. Xie, K. Zheng, X. Wu, J. Huo, Tuning the structural distortion and visible-light-driven photocatalytic properties of LaCoO<sub>3</sub> thin films by epitaxial strain, *J. Alloy. Compd.* 777 (2019) 679–687.

[21] C. Pan, Z. Wang, Y. Lou, Y. Zhang, Y. Dong, Y. Zhu, The construction of a wide-spectrum-responsive and high-activity photocatalyst,  $\text{Bi}_{25}\text{Co}_{40}$ , via the creation of large external dipoles, *J. Mater. Chem. A* 9 (2021) 3616–3627.

[22] S.J. Clark, M.D. Segall, C.J. Pickard, P. Hasnip, M. Probert, K. Refson, M.C. Payne, First principles methods used with CASTEP, *Z. Krist. Cryst. Mater.* 220 (2005) 567–570.

[23] J. Janek, M. Martin, K.D. Becker, Physical chemistry of solids—the science behind materials engineering, *Phys. Chem. Chem. Phys.* 11 (2009), 3010–3010.

[24] K. Fujita, T. Kawamoto, I. Yamada, O. Hernandez, H. Akamatsu, Y. Kumagai, F. Oba, P. Manuel, R. Fujikawa, S. Yoshida, M. Fukuda, K. Tanaka, Perovskite-type InCoO<sub>3</sub> with low-spin Co(3+): effect of In-O covalency on structural stabilization in comparison with rare-earth series, *Inorg. Chem.* 56 (2017) 11113–11122.

[25] C. Lv, G. Chen, X. Zhou, C. Zhang, Z. Wang, B. Zhao, D. Li, Oxygen-induced Bi(5+)-self-doped  $\text{Bi}_4\text{V}_2\text{O}_{11}$  with a p-n homojunction toward promoting the photocatalytic performance, *ACS Appl. Mater. Interfaces* 9 (2017) 23748–23755.

[26] G. Viruthagiri, P. Kannan, Visible light mediated photocatalytic activity of cobalt doped Bi<sub>2</sub>O<sub>3</sub> nanoparticles, *J. Mater. Res. Technol.* 8 (2019) 127–133.

[27] Dhruvashi, P.K. Shishodia, Effect of cobalt doping on ZnO thin films deposited by sol-gel method, *Thin Solid Films* 612 (2016) 55–60.

[28] Y. Hu, D.C. Sinclair, Relaxor-like dielectric behavior in stoichiometric sillenite  $\text{Bi}_{12}\text{SiO}_{20}$ , *Chem. Mater.* 25 (2012) 48–54.

[29] Y. Kumar, A. Sahai, S.F. Olive-Méndez, N. Goswami, V. Agarwal, Morphological transformations in cobalt doped zinc oxide nanostructures: effect of doping concentration, *Ceram. Int.* 42 (2016) 5184–5194.

[30] Y. Kawakami, K. Inoue, A. Kaneta, K. Okamoto, M. Funato, Quantification of the internal quantum efficiency in GaN via analysis of the heat generated by non-radiative recombination processes, *J. Appl. Phys.* 117 (2015), 105702.

[31] X. Wang, Y. He, Y. Hu, G. Jin, B. Jiang, Y. Huang, Photothermal-conversion-enhanced photocatalytic activity of flower-like CuS superparticles under solar light irradiation, *Sol. Energy* 170 (2018) 586–593.

[32] R. Wang, G. Shan, T. Wang, D. Yin, Y. Chen, Photothermal enhanced photocatalytic activity based on Ag-doped CuS nanocomposites, *J. Alloy. Compd.* 864 (2021), 158591.

[33] B. He, S. Jia, M. Zhao, Y. Wang, T. Chen, S. Zhao, Z. Li, Z. Lin, Y. Zhao, X. Liu, General and robust photothermal-heating-enabled high-efficiency photoelectrochemical water splitting, *Adv. Mater.* 33 (2021) 2004406.

[34] S. Cai, J. Li, E. Yu, X. Chen, J. Chen, H. Jia, Strong photothermal effect of plasmonic Pt nanoparticles for efficient degradation of volatile organic compounds under solar light irradiation, *ACS Appl. Nano Mater.* 1 (2018) 6368–6377.

[35] S. Yao, J. Wu, W. Li, R. Zheng, R. Li, Y. Chen, J. Luo, X. Zhou, LaCoO<sub>3</sub> co-catalyst modified Ag<sub>2</sub>CrO<sub>4</sub> for improved visible-light-driven photocatalytic degradation of tetracycline, *Sep. Purif. Technol.* 227 (2019), 115691.

[36] Y. Ding, P. Zhou, H. Tang, Visible-light photocatalytic degradation of bisphenol A on NaBiO<sub>3</sub> nanosheets in a wide pH range: a synergistic effect between photocatalytic oxidation and chemical oxidation, *Chem. Eng. J.* 291 (2016) 149–160.

[37] S. Yu, Y. Zhang, M. Li, X. Du, H. Huang, Non-noble metal Bi deposition by utilizing Bi<sub>2</sub>WO<sub>6</sub> as the self-sacrificing template for enhancing visible light photocatalytic activity, *Appl. Surf. Sci.* 391 (2017) 491–498.

[38] H. Sun, S. Liu, G. Zhou, H.M. Ang, M.O. Tade, S. Wang, Reduced graphene oxide for catalytic oxidation of aqueous organic pollutants, *ACS Appl. Mater. Interfaces* 4 (2012) 5466–5471.

[39] H. Fu, C. Pan, W. Yao, Y. Zhu, Visible-light-induced degradation of rhodamine B by nanosized Bi<sub>2</sub>WO<sub>6</sub>, *J. Phys. Chem. B* 109 (2005) 22432–22439.

[40] R. Wang, X. Ma, T. Liu, Y. Li, L. Song, S.C. Tjong, L. Cao, W. Wang, Q. Yu, Z. Wang, Degradation aspects of endocrine disrupting chemicals: a review on photocatalytic processes and photocatalysts, *Appl. Catal. A Gen.* 597 (2020), 117547.

[41] D. Dolat, N. Quici, E. Kusiak-Nejman, A.W. Morawski, G. Li, Puma, one-step, hydrothermal synthesis of nitrogen, carbon co-doped titanium dioxide (N,C-TiO<sub>2</sub>) photocatalysts. Effect of alcohol degree and chain length as carbon dopant precursors on photocatalytic activity and catalyst deactivation, *Appl. Catal. B Environ.* 115–116 (2012) 81–89.

[42] J. Ángelo, P. Magalhães, L. Andrade, A. Mendes, Characterization of TiO<sub>2</sub>-based semiconductors for photocatalysis by electrochemical impedance spectroscopy, *Appl. Surf. Sci.* 387 (2016) 183–189.

[43] N. Baram, Y. Ein-Eli, Electrochemical impedance spectroscopy of porous TiO<sub>2</sub> for photocatalytic applications, *J. Phys. Chem. C* 114 (2010) 9781–9790.

[44] M.A. Melo Jr., Z. Wu, B.A. Nail, A.T. De Denko, A.F. Nogueira, F.E. Osterloh, Surface photovoltaic measurements on a particle tandem photocatalyst for overall water splitting, *Nano Lett.* 18 (2018) 805–810.

[45] Y. Wang, W. Jiang, W. Luo, X. Chen, Y. Zhu, Ultrathin nanosheets g-C<sub>3</sub>N<sub>4</sub>@Bi<sub>2</sub>WO<sub>6</sub> core-shell structure via low temperature reassembled strategy to promote photocatalytic activity, *Appl. Catal. B Environ.* 237 (2018) 633–640.

[46] P. Han, D.M. Bartels, Temperature dependence of oxygen diffusion in H<sub>2</sub>O and D<sub>2</sub>O, *J. Phys. Chem.* 100 (1996) 5597–5602.

[47] Z. Cui, H. Jiang, Theoretical investigation of Ta<sub>2</sub>O<sub>5</sub>, TaON, and Ta<sub>3</sub>N<sub>5</sub>: electronic band structures and absolute band edges, *J. Phys. Chem. C* 121 (2017) 3241–3251.

[48] D. Liu, J. Wang, X. Bai, R. Zong, Y. Zhu, Self-assembled PDINH supramolecular system for photocatalysis under visible light, *Adv. Mater.* 28 (2016) 7284–7290.

[49] D. Chen, J. Yang, Y. Zhu, Y. Zhang, Y. Zhu, Fabrication of BiOI/graphene Hydrogel/FTO photoelectrode with 3D porous architecture for the enhanced photoelectrocatalytic performance, *Appl. Catal. B Environ.* 233 (2018) 202–212.

[50] C. Pan, R.G. Nuzzo, A.A. Gewirth, ZnAl<sub>x</sub>Co<sub>2-x</sub>O<sub>4</sub> spinels as cathode materials for non-aqueous Zn batteries with an open circuit voltage of  $\leq 2$  V, *Chem. Mater.* 29 (2017) 9351–9359.

[51] C.J. Venegas, E. Yedinak, J.F. Marco, S. Bollo, D. Ruiz-León, Co-doped stannates/reduced graphene composites: Effect of cobalt substitution on the electrochemical sensing of hydrogen peroxide, *Sens. Actuators B Chem.* 250 (2017) 412–419.

[52] S.C. Petitto, E.M. Marsh, G.A. Carson, M.A. Langell, Cobalt oxide surface chemistry: the interaction of CoO(100), Co<sub>3</sub>O<sub>4</sub>(110) and Co<sub>3</sub>O<sub>4</sub>(111) with oxygen and water, *J. Mol. Catal. A Chem.* 281 (2008) 49–58.

[53] S.A. Lourenço, R.S. Silva, A.C.A. Silva, N.O. Dantas, Structural and optical properties of Co<sup>2+</sup>-doped PbSe nanocrystals in chalcogenide glass matrix, *J. Phys. Chem. C* 119 (2015) 13277–13282.

[54] A. Niemöller, P. Jakes, R.-A. Eichel, J. Granwehr, In operando EPR investigation of redox mechanisms in LiCoO<sub>2</sub>, *Chem. Phys. Lett.* 716 (2019) 231–236.

[55] R. Martínez-García, M. Knobel, G. Goya, M.C. Giménez, F.M. Romero, E. Reguera, Heat-induced charge transfer in cobalt iron cyanide, *J. Phys. Chem. Solids* 67 (2006) 2289–2299.

[56] N. Shimamoto, S.-i. Ohkoshi, O. Sato, K. Hashimoto, Control of charge-transfer-induced spin transition temperature on cobalt–iron prussian blue analogues, *Inorg. Chem.* 41 (2002) 678–684.

[57] L. Liao, Q. Zhang, Z. Su, Z. Zhao, Y. Wang, Y. Li, X. Lu, D. Wei, G. Feng, Q. Yu, X. Cai, J. Zhao, Z. Ren, H. Fang, F. Robles-Hernandez, S. Baldelli, J. Bao, Efficient solar water-splitting using a nanocrystalline CoO photocatalyst, *Nat. Nanotechnol.* 9 (2014) 69–73.

[58] D. Long, X. Li, Z. Yin, S. Fan, P. Wang, F. Xu, L. Wei, M.O. Tadé, S. Liu, Novel Co<sub>3</sub>O<sub>4</sub> @ CoFe<sub>2</sub>O<sub>4</sub> double-shelled nanoboxes derived from Metal–Organic Framework for CO<sub>2</sub> reduction, *J. Alloy. Compd.* 854 (2021), 156942.

[59] J.H. Joshi, D.K. Kanchan, M.J. Joshi, H.O. Jethva, K.D. Parikh, Dielectric relaxation, complex impedance and modulus spectroscopic studies of mix phase rod like cobalt sulfide nanoparticles, *Mater. Res. Bull.* 93 (2017) 63–73.

[60] J. Li, L. Cai, J. Shang, Y. Yu, L. Zhang, Giant enhancement of internal electric field boosting bulk charge separation for photocatalysis, *Adv. Mater.* 28 (2016) 4059–4064.

[61] Z. Zhang, X. Chen, H. Zhang, W. Liu, W. Zhu, Y. Zhu, A highly crystalline perylene imide polymer with the robust built-in electric field for efficient photocatalytic water oxidation, *Adv. Mater.* 32 (2020) 1907746.

[62] F. Le Formal, K. Sivula, M. Grätzel, The transient photocurrent and photovoltage behavior of a hematite photoanode under working conditions and the influence of surface treatments, *J. Phys. Chem. C* 116 (2012) 26707–26720.

[63] Y. Zhu, X. Ma, Y. Xu, X. Chen, Large dipole moment induced efficient bismuth chromate photocatalysts for wide-spectrum driven water oxidation and complete mineralization of pollutants, *Natl. Sci. Rev.* 7 (2020) 652–659.